Measured and modeled acoustic propagation underneath the rough Arctic sea-ice

Gaute Hope,[a] Hanne Sagen, Espen Storheim, and Halvor Hobæk
Nansen Environmental and Remote Sensing Center, Bergen, Norway

Lee Freitag
Woods Hole Oceanographic Institution, Woods Hole, Massachusetts 02543, USA

(Received 13 October 2016; revised 17 August 2017; accepted 6 September 2017; published online 26 September 2017)

A characteristic surface duct beneath the sea-ice in the Marginal Ice Zone causes acoustic waves to be trapped and continuously interact with the sea-ice. The reflectivity of the sea-ice depends on the thickness, the elastic properties, and its roughness. This work focuses on the influence of sea-ice roughness on long-range acoustic propagation, and on how well the arrival structure can be predicted by the full wave integration model OASES. In 2013, acoustic signals centered at 900 Hz were transmitted every hour for three days between ice-tethered buoys in a drifting network in the Fram Strait. The experiment was set up to study the signal stability in the surface channel below the sea-ice. Oceanographic profiles were collected during the experiment, while a statistical description of the rough sea-ice was established based on historical ice-draft measurements. This environmental description is used as input to the range independent version of OASES. The model simulations correspond fairly well with the observations, despite that a flat bathymetry is used and the sea-ice roughness cannot be fully approximated by the statistical representation used in OASES. Long-range transmissions around 900 Hz are found to be more sensitive to the sea-ice roughness than the elastic parameters. © *2017 Acoustical Society of America*. [http://dx.doi.org/10.1121/1.5003786]

[NPC] Pages: 1619–1633

I. INTRODUCTION

The Marginal Ice Zone (MIZ) is the region between the fully ice-covered areas and open water that exists in the polar regions of the world. The shape, extent and size distribution of floes within the MIZ area are determined by ocean swell propagating across the ice edge and several tens of kilometers into the ice pack. Local winds and mesoscale ocean processes, such as eddies, will shape the ice edge to be diffuse or compact (e.g., Johannessen *et al.*[1]). The MIZ exists within the *seasonal ice zone*, the area between the summer minimum and the winter maximum, but its extent at any given time varies with the season and is undergoing changes according to recent satellite data analysis.[2]

As the size of the seasonal ice zone increases due to the reduction in summer ice coverage, the MIZ spans larger regions within the polar seas. The size and composition of the MIZ varies with location, and the Greenland, Labrador, and Bering Seas all have different characteristics that are influenced by regional oceanographic features, wind, and wave conditions.[3] Recent studies in the Canada Basin reveal what has been described as a "thermodynamically forced MIZ," of melt ponds and deteriorating ice that impact the temperature and salinity of the upper layers.[4]

The structure of the ocean beneath the sea-ice is characterized by a 100–200 m deep, cold, and fresh layer. This surface layer thins toward the edge of the ice. From an acoustic perspective, this cold, freshwater layer under the ice forms a shallow surface duct, which traps acoustic waves above a cut-off frequency and causing them to repeatedly interact with the underside of the sea-ice (e.g., Jensen *et al.*[5]). The varying sea-ice characteristics of the MIZ, the near-surface stratification and horizontal variation govern how acoustic signals propagate in the MIZ.

A number of previous acoustic experiments have been carried out at frequencies between 200–300 Hz in the MIZ between Greenland and Svalbard. The short-term acoustic experiments in the 1980s during the "Marginal Ice Zone Experiment" were carried out to learn more about the ice-ocean processes, ambient noise (Johannessen *et al.*[1]), and acoustic propagation (Dyer *et al.*,[6] Dahl *et al.*[7]).

In the Greenland Sea tomography experiment in 1988–1989 (Worcester *et al.*[8]), signals of 250 Hz were transmitted in an area that was seasonally covered by sea ice. As part of this scientific program, a modeling study was carried out to investigate the reflection and scattering from the ice cover at 250 Hz (Jin *et al.*[9]). The study found that the observed amplitude reduction in the acoustic receptions was indeed caused by the sea ice, and in particular the shear wave parameters of the ice. It was also observed that the damping of the acoustic signal is sensitive to the details of the ocean mixed layer.

However, most of the attempts to model acoustic propagation across the ice edge included significant simplifications of the physical conditions by ignoring or approximating the effect of sea ice (e.g., Mellberg *et al.*,[10] Sagen *et al.*[11]). The effect of a discontinuous ice cover and strong gradients in the ocean, which is often found in the outer part of the MIZ, and sometimes within the pack ice, has only been addressed by a few investigators (e.g., Dahl,[12] Fricke[13]).

[a]Electronic mail: gaute.hope@nersc.no

In the fully ice covered regions, the ocean is more stratified, but also more stable in time and space. This results in more temporal dispersal of the signal, which means the multi-path arrivals are better resolved due to spread. This was explored in the trans Arctic Experiments in the 1990s where 20 Hz signals were sent across the Arctic Basin to demonstrate the possibilities of acoustic thermometry (e.g., Mikhalevsky *et al.*[14]). It was also found that the loss due to sea ice is highly frequency-dependent, increasing exponentially with frequency, and thereby creating a low-pass filter (e.g., Diachok,[15] Mikhalevsky[16]).

In the PRUDEX experiment (ice camp in 1987), coupling of seismo-acoustic waves from explosives under the ice to the sea ice was investigated using recordings from geophones and hydrophone arrays (Miller and Schmidt[17]). It was found that the shear wave attenuation of the sea-ice is the most important parameter for the reflection of acoustic waves, and this conclusion is also supported by Fricke.[13] McCammon and McDaniel[18] found that the shear wave attenuation is important for incidence angles between 20° and 60°. Diachok[15] studied the effect of sea-ice ridges on reflection loss, noting that for rays traveling longer than 30 km the incidence angles were generally greater than 75°.

The main difficulty in modeling sound propagation in ice-covered regions is inclusion of the reflection and scattering from rough elastic surfaces.[13,19] LePage and Schmidt[19] modeled the transmission loss of low-frequency propagation in the Arctic (<100 Hz) using SAFARI (the predecessor to OASES), and the method of small perturbations (MSP) to characterize the ice roughness (Kuperman and Schmidt[20]). They showed that their model agreed fairly well with observations of transmissions across the Arctic for those frequencies.

The full-wave model OASES[21] is currently the model that best handles the rough sea-ice cover, although it is less well-suited for range-dependent studies of the ocean because these studies require a relatively smooth horizontal variation. To study the impact of typical gradients in the ocean parameters, it is more convenient to use ray models, and models based on parabolic approximations (Jensen *et al.*[5]).

In 2010, Woods Hole Oceanographic Institution (WHOI) carried out an acoustic communication experiment inside the ice-covered MIZ of the Fram Strait.[22] The goal of the experiment was to study the range and reliability of acoustic communications in the MIZ. This study showed that it was feasible to transmit data at frequencies of 700 and 900 Hz over 10–100 km in this area of the Arctic. However, it also raised questions about the mechanisms of loss in the MIZ, helping to motivate an additional experiment and the analysis presented here.

This paper focuses on the effect of sea-ice roughness on propagation of specific acoustic signals centered at 900 Hz. This is done by analyzing signals transmitted under the sea-ice and compare them with acoustic modeling results using the OASES modeling package.[21] The signals were transmitted in the Fram Strait inside the Marginal Ice Zone in September 2013 as part of the UNDER-ICE field program.

Section II provides details about experiment setup and transmitted signals. In Sec. III the ocean parameters measured during the experiment, and historical ice draft measurements, are used to create an acoustical model with rough sea-ice as input to OASES. The effect on signal propagation of including smooth sea-ice and rough sea-ice is addressed in a sequence of simulation experiments in Sec. IV. In Sec. V the received signals are analyzed and in Sec. VI the observations are compared qualitatively with the model simulations. Effect of sea-ice roughness on acoustic signals and limitations of modeling and approach are discussed. Finally, a summary and concluding remarks are provided in Sec. VII.

II. EXPERIMENT CONFIGURATION

A. Experiment

In September 2013, two ice tethered buoys were deployed on the sea-ice in the Fram Strait near 82°N and 0°E, as a part of the acoustic communication experiment. The buoys, referred to as *WHOI1* and *WHOI2*, were equipped with a Geospectrum Technologies source suspended at approximately 90 m depth. The source signal was a frequency modulated (FM) sweep with a center frequency of $f_c = 900$ Hz, and variable bandwidth from 10 to 100 Hz with corresponding duration from $T = 20$ to 2 s.

A third drifting observation platform, an "Integrated Ice Station" (*IIS*) was deployed 32 km further south on the sea-ice as part of UNDER-ICE led by NERSC. *IIS* was equipped with a four element hydrophone array to record ambient noise data (Geyer *et al.*[23]) and to receive the signals transmitted from the buoys.

The *IIS* was deployed on the 14th of September at 81°45′ N, 1°49′ W on an ice floe 20 km from the ice edge, and recovered four days later at 81°20′ N, 1°42′W, 46 km from the deployment position. Transmissions were made every hour according to a fixed schedule, resulting in a set of 72 transmission. Of these, the signals with bandwidth of $\Delta f = 25$ Hz, between the *WHOI1* buoy and the *IIS* station, will be the focus of this analysis, since this path and bandwidth contained the most measurements and the best discernible multi-path arrival structure.

The receiver station (*IIS*) was equipped with a vertical receiver array of four High Tech Inc. HTI-90-U hydrophones. These were mounted at 15, 20, 25 m, and 30 m depth. The hydrophones have a nominal frequency response from 2 Hz to 20 kHz, but have a built-in high-pass filter at 10 Hz to reduce the effect of strumming. The sampling frequency was 3906.25 Hz, and recording was performed continuously over the course of the entire experiment.

Figure 1 shows the geometry of the experiment as the buoys were drifting southward with the sea ice. The satellite image shows the sea-ice extent on 14 September 2013. The solid lines represent the ice edge determined from satellite images taken each day during the deployment. Each buoy was equipped with a Global Positioning System receiver (GPS) logging its position. The colors used for the buoy positions and the ice edge correspond to the different days of the drift. The green squares along 82° N show the XCTD casts that were made.

The relative distance between the buoys remained fairly constant during the experiment, indicating that the sea ice

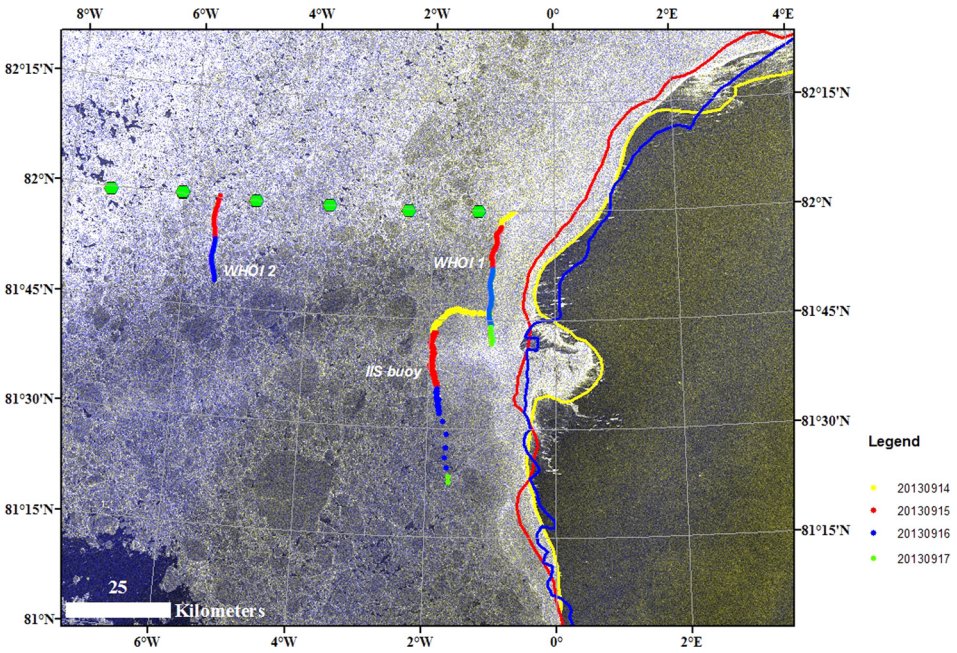

FIG. 1. (Color online) Deployment setup and drift path of the buoys. *WHOI1* and *WHOI2* transmitted signals between each other, which were recorded by *IIS*. The satellite image shows the sea-ice on the 14 September 2013. The varying ice edge for the days 14, 15, and 16 September is shown. The shade of the ice edge and the buoy drift track indicate which day it represents. XCTD casts made during the experiment are marked with circles along 82° N. Figure modified from Geyer *et al.* (Ref. 23).

drifted southward with little deformation or rotation. While *WHOI1* and *IIS* moved parallel with the ice edge, some compression and westward movement of the ice edge is seen on the 14th around 81° 35′ N.

The GPS receiver provided timing and position for the buoys. However, due to clock skew and poor GPS reception the transmission times and positioning are not accurate enough to calculate absolute and relative travel times. Thus our focus is on the arrival structure and its variability, with respect to sea-ice surface conditions, rather than analyzing changes in travel time.

B. Signal processing

The records containing the received signals are extracted from the complete recording based on the known transmission schedule. The signals are then processed using standard matched filter (pulse compression) techniques. First, the signal is demodulated to base-band, decimated so that the sampling corresponds to the maximum frequency of the matched filter, and filtered with the base-band template sweep. A Hamming-window is applied to the matched filter template to avoid ringing and reduce side-lobes. The gain obtained by pulse-compression[24] of the sweep with $T = 8$ s and $\Delta f = 25$ Hz is $H = \sqrt{T \cdot \Delta f} \approx 23$ dB.

Figure 2 shows 9-s segments of the recordings after matched filter processing, where the processed signal from each hour is stacked vertically, starting with the first transmission at the bottom. The amplitude shown is corrected for pulse-compression gain.

The transmissions were turned off at some hours (e.g., hour 8 and 23) due to conflicting experiments, this results in noisy or quiet traces in Fig. 2 as the matched filter may pick up other signals. The traces are included here for completeness.

The receptions are characterized by a strong first arrival, seen near 21.5 s for the first 6 h, with weaker arrivals following. The arrival time is stable until 27 h since deployment, after which the arrival time increases approximately linearly with increased range until it slows down at approximately 60 h.

C. Bathymetry

The bathymetry between the transmitting and receiving buoy is obtained from the International Bathymetric Chart of the Arctic Ocean[25] (IBCAO) and shown in the right panel of Fig. 2. The right edge of the contours indicates the distance between the two buoys. The experiment was carried out over the Yermak plateau, north of Svalbard. Upon deployment, the shallowest point (1600 m depth) along the transect is located between the buoys. As the buoys drift southward, the transmitting buoy crosses the shallowest part (between 26 and 49 h after deployment), before both the transmitting and receiving buoy drift out above the slope falling down toward the deep Fram Strait (maximum 3200 m depth).

For the first 36 h after deployment, the distance varies from 31.9 to 35 km, which corresponds to an average increase of 86 m per hour. From 36 to 58 h after deployment the increase is more rapid, from 35 to 39 km, or 180 m/h. Finally, it slows down to 140 m/h for the last 2 km over the next 14 h as the distance increases to 41 km.

D. Sound speed

Sound speed profile measurements in the region was performed by XCTD casts approximately every 10 nm along 82° N from 7° W to 1° W, with a total of six measurements along a 94 km long transect. Figure 3 shows the raw data from the measurements along the transect. The western-most probe terminated at a shallower depth because of the wire getting tangled in strong currents or getting in contact with the sea-ice.

A mean sound speed profile $\overline{c_w}(z)$ is calculated from these measurements (shown in Fig. 3). Two potential surface channels are seen from the steep gradients in the sound speed: one with a depth of 100 m; and the other with a depth of approximately 220 m. These channels arise due to the cold,

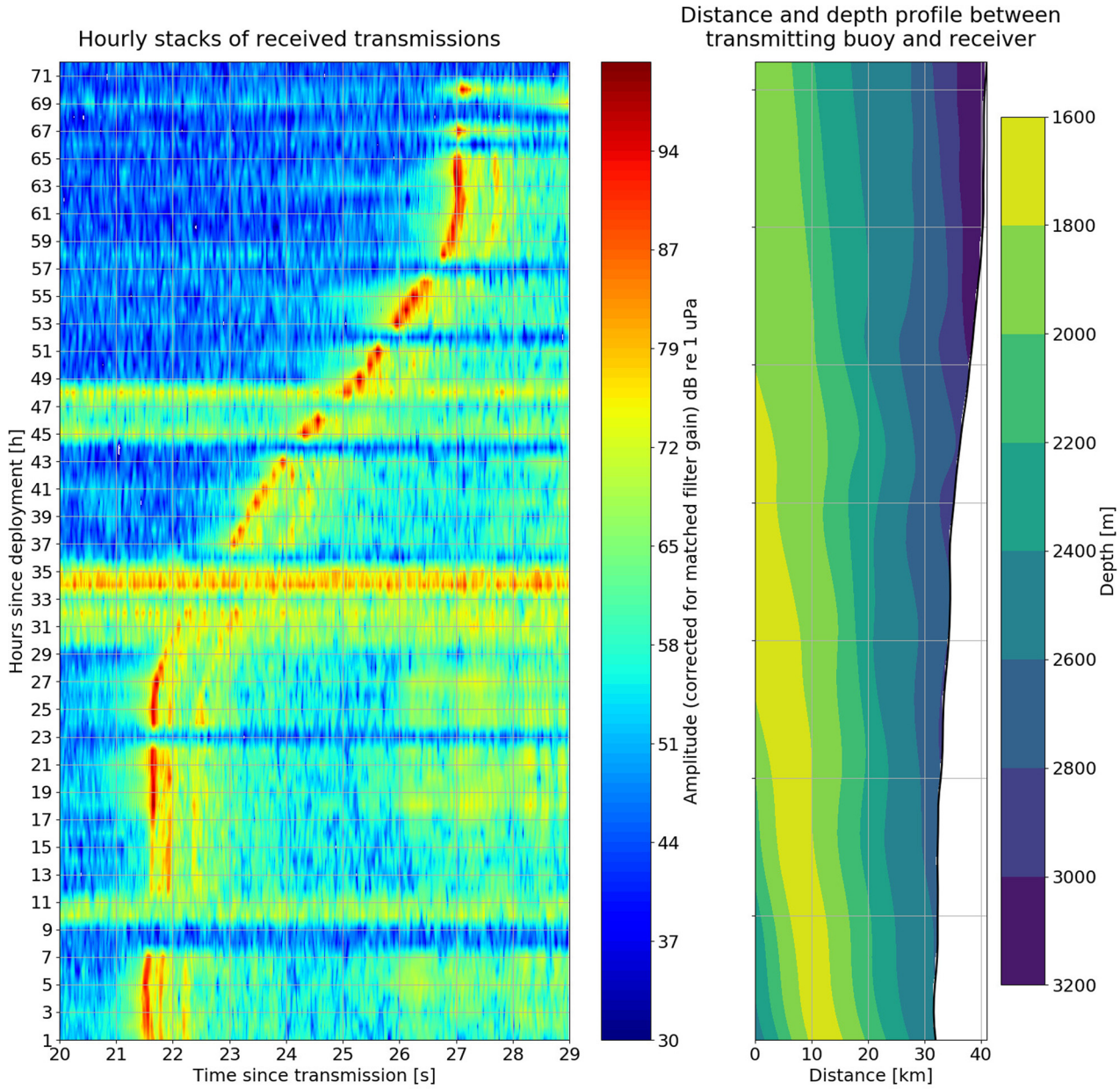

FIG. 2. (Color online) Left panel show the 72 received signals (matched filter output) from *WHOI1* to *IIS*, $\Delta f = 25$ Hz, $f_c = 900$ Hz, stacked with first transmission at the bottom. The right panel shows the bottom topography between transmitting and receiving buoy as the system drifts southward off the Yermak plateau and onto the east facing slope toward the Fram Strait. The same signals were sent each hour. The 9-s segments are shown stacked vertically, with the first transmission at the bottom and last transmission (after 72 h) at the top.

fresh water underneath the ice. The slowest sound speed is $c_0 = 1435$ m/s, located near the surface. The sound speed is relatively constant from 220 m down to approximately 650 m, after which it increases linearly as a function of pressure.

A surface channel generally acts as a high-pass filter, where sound above a certain cutoff frequency will be trapped in the channel. This frequency, for an isothermal surface channel with depth D and sound speed c_d, is given by Eq. (1.36) from Jensen *et al.*:[5]

$$f_0 \simeq \frac{c_d}{0.008 \cdot D^{3/2}}.$$

Using $c_d = c_0 = 1435$ m/s, the cutoff frequency is approximately 55 Hz for $D = 220$ m, while $D = 100$ m gives a 180 Hz cutoff frequency. These are both well below the source frequencies used in this work and a large part of the signal used here will propagate inside the surface channel.

III. MODEL SETUP

Modeling is performed with the range-independent version of OASES. The model consists of a layer of water enclosed above by a sea-ice layer with a vacuum half-space on top, and below by a sea-floor half-space.

A. Ocean

The mean sound speed profile measured using XCTDs is used to make a 12 point linear, piece-wise model as input

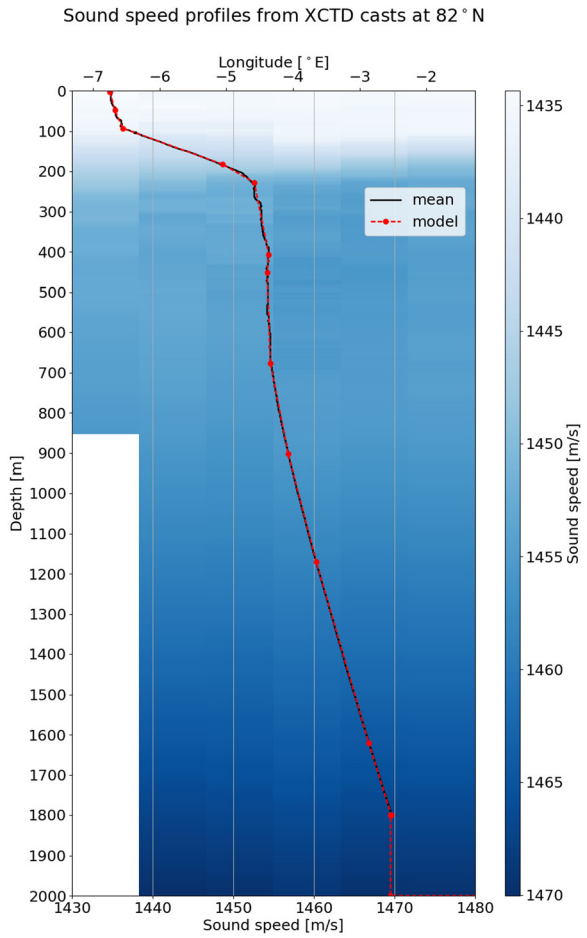

FIG. 3. (Color online) Sound speed profile from 82° N used in model. The line with circles shows the discretized model overlaid the mean sound speed profile, calculated from XCTDs collected during the *UNDER-ICE 2013* cruise. The background image shows the sound speed calculated for each of the 6 casts between 7° W to 1° W.

to OASES. Figure 3 shows the model overlaid the mean sound speed as a dashed line with each interface marked with circles. The number of points is chosen in order to capture the most important features of the mean profile, while limiting the number of interfaces, and consequently, the computational time.

The attenuation in the water is calculated using Eq. (1.47) from Jensen *et al.*,[5] which for 900 Hz is $\alpha_w = 0.06$ dB/km.

B. Seafloor

The bathymetry in the model has a constant depth of $z_b = 2000$ m. The elastic parameters of the visco-elastic seafloor are listed in Table I, where subscript p and s indicate longitudinal and shear, respectively. These properties are based on seismic observations from the Fram Strait.[26]

C. Sea-ice thickness and roughness

In OASES the sea-ice is represented as a sea-ice layer replacing a part of the uppermost layer with a either a smooth or rough water-ice boundary. The upper boundary of the sea-ice is smooth, with a vacuum half-space above. The

TABLE I. A simplified, reflective, seafloor with elastic parameters compiled from Jokat *et al.* (Ref. 26) is used in the model. Λ denotes spatial wavelength.

Depth	c_p	c_s	α_p	α_s	ρ
2000 m	2200 m/s	1500 m/s	0.5 dB/Λ	0.5 dB/Λ	2.9 kg/dm^3
2200 m	3500 m/s	1500 m/s	0.5 dB/Λ	0.5 dB/Λ	2.9 kg/dm^3

roughness is implemented in OASES using the method of small perturbations (MSP),[20] with the sea-ice layer given in terms of a mean ice-thickness of $\bar{h}_{ice}$, a RMS variation around the mean, and a characteristic correlation length (CL).

The underside of the ice in the Arctic consists of strongly varying shapes such as ridges, edges, stacked ice-floes or tunnels. The ice is constantly under the influence of ocean currents, wind and freeze-melt processes and can move more than 40 km in a day.[27] Being subjected to compression, decompression and opening of leads, the underside of the sea-ice is constantly changing. A detailed map is therefore not possible to make, nor would it be very useful since it would be invalidated in a short time. A statistical model is therefore used in OASES to parameterize the sea-ice so that it can be modeled.

The method of small perturbations in OASES can handle roughness with a RMS variation that is small compared to the wavelength.[28] At 900 Hz the wavelength in water (1435 m/s) is $\lambda_w = 1.59$ m, while $\lambda_p = 4.00$ m and $\lambda_s = 2.00$ m in the sea-ice. Existing measurements of sea-ice roughness suitable for acoustic modeling are very sparse. DiNapoli and Mellen[29] measured the RMS roughness to be 1.9 m (mean thickness 3.9 m), and characteristic correlation length to be 44.8 m. These were used by Kuperman and Schmidt[30] for their numerical modeling experiments of Arctic propagation for frequencies of 100 Hz and below.

The ice thickness distribution (shown in Fig. 4), RMS, and characteristic correlation length were calculated for one segment in the Nansen basin (84.1° N, 25.2° E) measured in

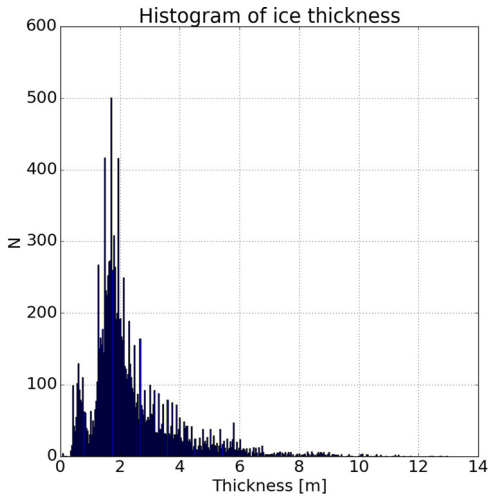

FIG. 4. (Color online) Histogram of ice-thickness distribution computed from National Snow and Ice Data Center 31. The distribution is used as parameters for sea-ice roughness in OASES (Table IV).

2005 by a submarine with upward looking sonar (distributed by the National Snow and Ice Data Center[31]). The segment of ice drafts closest to our area was chosen, however this is still 440 km further north and 8 years earlier. The segment consists of almost equidistant samples, except for a few gaps of missing measurements. In order to calculate the autocorrelation function (ACF), equidistant sampling is required. The full segment is split at each data gap, so that each sub-segment now consists of almost equidistant measurements. The autocorrelation functions for each sub-segment is then calculated. The ACFs are combined by summing the overlapping lags of the ACFs, weighted with the number of samples in the sub-segment. The full segment is detrended before the RMS is calculated, and the characteristic correlation length is calculated from the combined ACF.[20,32] The mean ice-thickness for this segment is 2.4 m, the standard deviation (or RMS with mean deducted) is 1.52 m, and the characteristic correlation length is 19.1 m.

A Gaussian distribution around the mean is used as model for the sea-ice thickness in OASES. As can be seen in Fig. 4, this does not match the reality. This model also assumes the roughness to be isotropic and transversely invariant. While the roughness is likely to exhibit similar characteristics within the area of study, ice-keels extend along one direction and are therefore not isotropic. In OASES, only 2D transects are modeled and ice-keels or structures will therefore be sliced through, making their orientation, and clear contradiction with the simplified statistical model somewhat less important. At the same time, out of plane propagation is not accounted for. These approximations should be kept in mind while interpreting the effect of roughness.

The RMS value calculated from the upward looking sonar measurements (1.52 m) is too high compared to the wavelength at 900 Hz for it to be modeled with OASES using the MSP. It was therefore adjusted to a maximum of 0.6 m, a value where the reflection coefficient begin to show instabilities at low incidence angles. This is clearly a limitation in the model. However, it could be argued that the roughness is likely to be somewhat less than 1.52 m in our case since (1) the transmissions in this study are done in the end of the melting season, whereas the original measurements were done in November; (2) the area of the experiment is further south where the melting has been going on for a longer time; and (3) the general ice-thickness and amount of multi-year ice has decreased significantly since 2005.[33] Still, a maximum roughness in the model of 0.6 m RMS is an underestimate. A lower RMS value of 0.2 m is used to study the effect of reducing the roughness.

The closest and most recent ice-thickness measurements that match season and location were made in the Fram Strait in 2011.[33] These were made using a tethered upward looking sonar and measured a mean ice-thickness of 2.0 m. Only thickness is used from this data set since suitable roughness characteristics were unavailable.

D. Elastic parameters of sea-ice

The sea-ice is modeled as an elastic and isotropic layer, which is described by density, and the compressional, and shear speed with corresponding compressional and shear attenuation. However, this is a simplification since sea-ice consists of multiple layers meshed together forming fractures and internal structure of a potential wide range of compositions. The elastic parameters change throughout the season as the temperature of the ice changes, and the surrounding environment affects the internal structure. There can therefore be large variations in the reflection coefficient of the same ice-floe throughout the season.[34]

Obtaining measurements of the internal elastic parameters of the sea-ice is not trivial. Using cross-hole tomography of an ice-floe Rajan *et al.*[35] were able to produce a detailed image of the internal sound speeds of one ice-floe in the Beaufort sea. Laible and Rajan[34] used these to produce a background model, which agrees well with previous and historical measurements of sound speed in sea-ice. This background model is judged to be the best starting point for modeling in this analysis (see Table II). However, large variations must be expected throughout the Arctic depending on each ice-floe's history (such as fracturing, stacking, melting, and refreezing) as well as on the conditions of the ocean water when the ice was formed.

The attenuation measured for the compressional wave by Rajan *et al.*[35] varies from 0.06 to 0.282 dB/m/kHz. These estimates were made for a signal at 30 kHz. Clee *et al.*[36] measured the attenuation at approximately 900 Hz to be about 0.115 dB/m/kHz, however these measurements were made on glacier ice. McCammon and McDaniel[18] gathered several measurements on attenuation for the purpose of modeling acoustic propagation in sea-ice. They arrived by linear regression at an attenuation of 0.06 dB/m/kHz, which is the same as the lower estimates by Rajan *et al.*[35] and those chosen by Laible and Rajan.[34] In this regression analysis, the values measured by Clee *et al.*[36] became outliers. The values measured by Rajan *et al.*[35] and computed by McCammon and McDaniel[18] are therefore considered to be the best estimate. The relation to shear wave attenuation is given by $\alpha_s = 6\alpha_p$.[18]

Hobæk and Sagen[37] modeled the reflection coefficient for several different cases of horizontally layered sea-ice, and found that the reflection coefficient is sensitive to attenuation. However, above 60° of incidence angles, the reflection coefficient nevertheless remains almost total (in particular for frequencies of 900 Hz). McCammon and McDaniel[18] found the shear attenuation to be the most important parameter for the reflection coefficient between incidence angles of 20° and 60°. It should be noted that for some models of

TABLE II. Average values from Rajan *et al.* (Ref. 35) as estimated by Laible and Rajan (Ref. 34), and McCammon and McDaniel (Ref. 18), was used as a model for the sea-ice layer.

Parameter	Value
c_p	3600 m/s (Ref. 34)
c_s	1800 m/s (Ref. 34)
ρ_{ice}	0.9 kg/dm^3 (Ref. 34)
α_p	0.06 dB/m/kHz (0.216 dB/Λ) (Refs. 18 and 35)
α_s	0.36 dB/m/kHz (0.648 dB/Λ) (Ref. 18)

porous fluid filled seafloors, the reflection coefficient may be reduced, in some cases even at high incidence angles.[38] If Biot theory[39,40] is used to model the sea-ice,[34] a lower reflection coefficient may be experienced. In this paper, an elastic model for the sea-ice is used.

IV. MODELING RESULTS

The OASES package was used to simulate four cases (Table III) based on Sec. III. The cases range from no sea-ice to rough sea-ice. The numerical parameters for the wave number integration of a model in OASES requires stabilization, but once it is stable, the model can be carefully perturbed without requiring re-stabilization.

A. Sea-ice reflection coefficient

Figure 5 shows the reflection coefficient calculated using OASES for the water-ice interface with 2 m smooth sea-ice (Case b in Table III) and for a sea-ice layer with 0.6 m RMS roughness (Case d), as a function of frequency and incidence angle. The black dashed line indicates 900 Hz. Increasing the thickness of the ice layer will compress the plot along the frequency axis, so that doubling the thickness of the ice layer to 4 m will cause the 900 Hz line to be moved down to where 450 Hz is now. The dips correspond to different modes of Rayleigh-Lamb waves for which an acoustic wave enters the ice.[37] Above 70° of incidence angle the reflection coefficient is almost total for the smooth ice (left). The reflection coefficient to the right in Fig. 5 accounts for scattering loss in the rough-sea ice case, in which case the reflection coefficient is dramatically changed, and the reflection is decreased for high angles of incidence. The white areas indicate regions where the reflection coefficient barely exceeds 1. This is a sign of instability in the model caused by the relatively high RMS value of 0.6 m compared to the wavelength. However, this occurs for frequencies and incidence angles not considered here.

Figure 6 shows the reflection coefficient for 900 Hz at incidence angles above 60°. The attenuation is varied along the ordinate, with a fixed proportion of $\alpha_s = 6\alpha_p$ between the shear and compressional attenuation. Increasing attenuation above 0.06 dB/m/kHz (i.e., value used in this work) does have an effect, in particular up to 75° angle of incidence. However, this effect is dwarfed by the effect of increasing the RMS roughness of the sea-ice to a, e.g., 0.6 m.

Figure 7 shows the distribution of incidence angles for all ray reflections at a fluid-vacuum surface interface, with rays modeled out to a range of 40 km with BELLHOP;[41] 7000 rays were launched with an angle of ±45° from a source at 90 m depth. All surface reflections are included in order to determine the number of interactions with the sea-ice, meaning that the total number of surface reflections is greater than the number of rays. The different colors indicate the turning point of the ray, with surface channel rays defined as those reaching a maximum depth of 250 m. Bottom reflected rays have one or more bottom reflections, while the rest are deep refracted rays. Most of the rays have incidence angles above 80°, with all rays that were trapped in the surface duct or refracted deeper having incidence angle above 75°. The setup is as for Case a, with the sound profile as shown in Fig. 3. Earlier literature found that most rays with incidence angles less than 73°–75° escape the Arctic surface duct[5,15] and will be refracted or reflected deeper, and therefore experience fewer bounces off the sea-ice over range.

TABLE III. Ice condition cases modeled using OASES.

Case	Ice thickness	RMS roughness	Characteristic correlation length
a	0 m	0 m	0 m
b	2 m	0 m	0 m
c	2 m	0.2 m	19.1 m
d	2 m	0.6 m	19.1 m

TABLE IV. Parameters for the Gaussian distribution used as model for the roughness of the underside of the sea-ice.

Parameter	Value
Mean ice thickness	2.0 m (Ref. 33)
RMS roughness	0.2 – 0.6 m
Characteristic correlation length	19.1 m (calculated from Ref. 31)

This distribution of incidence angles were computed for a surface interface which completely reflects the rays, showing that the shape of the distribution is a function of the sound speed profile and not the reflection coefficient at the surface.

The incidence angle of a plane wave is altered at a rough interface as a ridge or depression will change the inclination of the interface. However, the OASES model only considers the interface to be perturbed slightly (MSP) around a mean, plane, interface. This allows the roughness to be accounted for in the reflection coefficient (Fig. 6) and the incidence angle should be regarded as relative to a plane interface.

Waves at lower frequency or at a smaller angle of incidence will be affected more by the elastic parameters of the sea-ice. However, the setup and range in this experiment will contain waves with incidence angles generally above 75°. Above this angle the roughness is more significant than the elastic parameters for the reflection coefficient of the sea-ice.

B. Transmission loss

Figure 8 shows the magnitude of the coherent transmission loss (TL), using the range-independent OASES package, as a function of range and depth, for 900 Hz, from 0 to 120 km range, with 2 m smooth ice (upper panel), and 2 m thick ice with 0.6 m RMS roughness and 19.1 m correlation length (lower panel). The sea-ice interface corresponds to the reflection coefficients in Fig. 5. The sound speed profile is shown in the left column and is the same as shown in Fig. 3. The surface channel at approximately 100 m and a somewhat weaker channel at 220 m is visible.

The TL illustrates how the sound is distributed throughout the water column. Convergence zones causes the sound to be re-focused at regular spatial intervals near the surface at ranges of approximately 35, 70, and 105 km. In between

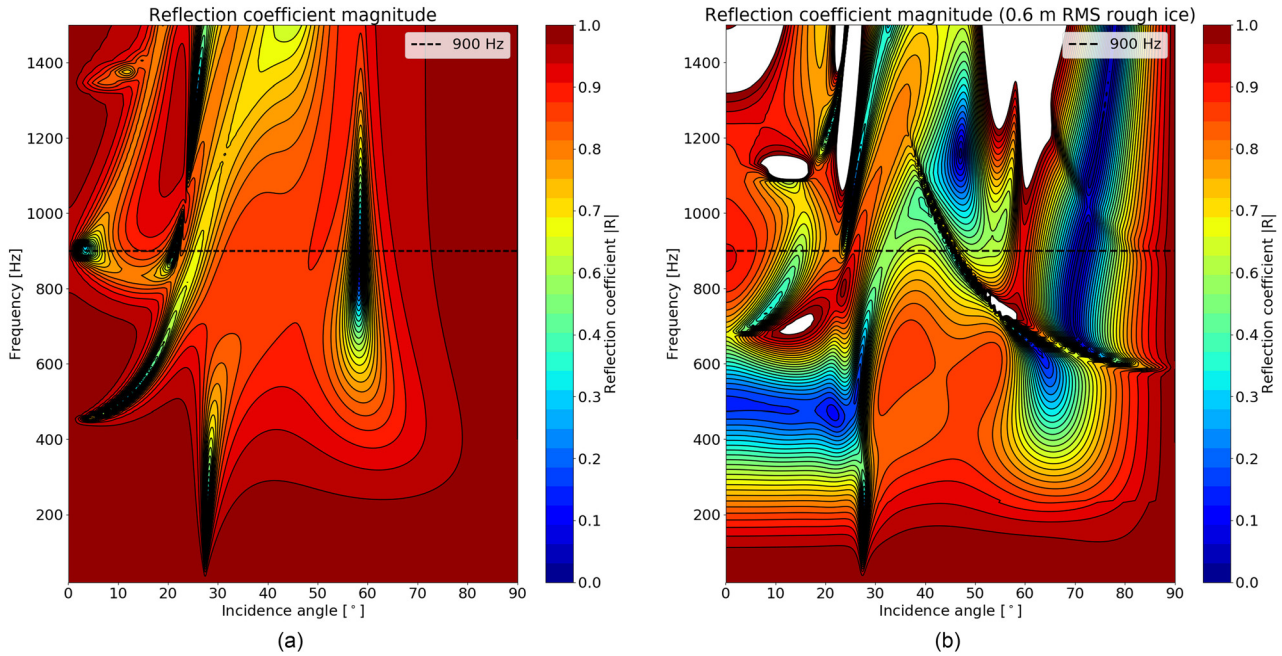

FIG. 5. (Color online) The left panel shows the reflection coefficient for a 2 m homogeneous, smooth, ice layer as described in Table II. The right panel shows the same layer with 0.6 m RMS deviations from the mean thickness. The frequency axis can be scaled with the thickness of the ice layer, causing the plot to be compressed proportionally along the frequency axis when the ice thickness is increased.

these high intensity regions, most of the energy extends down to approximately 1800 m depth. Bottom reflections are especially visible at ranges closer than 20 km.

A similar behavior is also observed for the case with no sea-ice. However, the reflection at the water/vacuum interface is total, independent of the incidence angle.

With rough ice the overall propagation is qualitatively similar as for smooth ice. However, there is a significantly higher attenuation with range, due to the scattering at the rough ice interface. Beyond 70 km range only the sound trapped in the shallowest surface channel ($D \approx 100$ m) is present, although weaker than for smooth sea-ice.

The sound speed profile is range dependent throughout the Arctic Ocean and across the Marginal Ice Zone. Acoustic signals propagated over long distances in the Arctic will interact with different ice conditions, open leads and changing sound speed in the ocean. Transmission loss is therefore determined by the scattering and reflection from the sea-ice, the dimension of the surface channel and the sound speed profile, and, in shallow water, reflectivity from the bottom.

Several different wave paths are visible in Fig. 8 that cause multiple arrivals, these will be studied through time domain analysis in Sec. IV C.

C. Time domain analysis

The transfer function between source and receiver is calculated using OASES for the frequency band 870–930 Hz. A source FM sweep from 900 Hz ± 12.5 (8 s) is then windowed using the Hamming window and transformed to the frequency domain. The received signal is found by multiplying the source spectrum with the transfer function and transforming the result back to the time domain. The simulated signal (FM-sweeps), in the time domain, is then processed using pulse-compression in the same way as the data (see Sec. II B).

Figure 9 shows the matched filter output of the simulated signal for increasing ranges ($r = 0$ to 120 km) as a function of reduced time $\tau = t - r/c_0$ at 30 m depth (no ice, Case a). $c_0 = 1435$ m/s corresponds to the lowest sound speed in

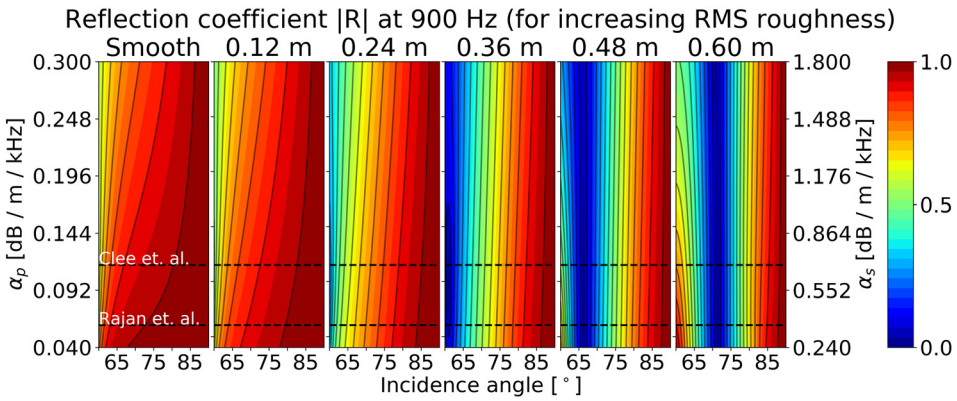

FIG. 6. (Color online) Attenuation vs roughness. The reflection coefficient for 900 Hz is plotted for increasing attenuation (vertical) vs increasing roughness (horizontal), for incidence angles between 60° and 90°.

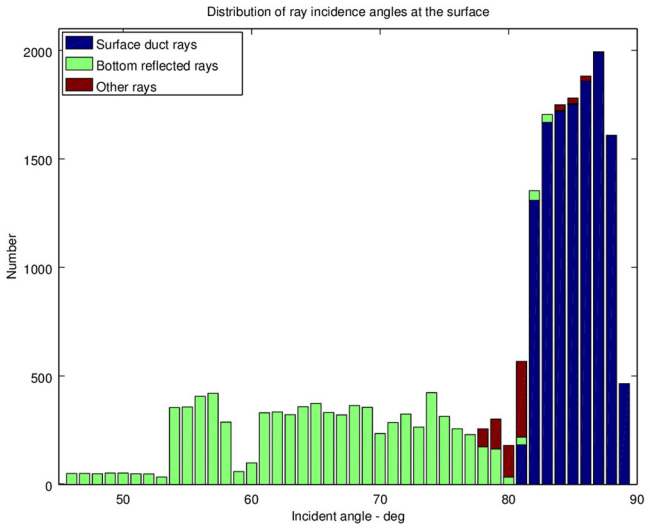

FIG. 7. (Color online) Distribution of ray reflection incidence angles with a plane vacuum interface for a source located at 90 m out to a range of 40 km. The majority of interactions have an incidence angle above 80°.

the surface channel. This causes the pulses to be shifted forward (leftward) with the travel-time at its range for the direct path in the surface channel, so that the vertical line (B) near $\tau = 0$ s is an arrival traveling with the same speed as the sound speed in the surface channel. The received signal at each range is stacked vertically, with the closest range at the bottom. Additionally, each signal has been scaled with $\sqrt{r}$ to compensate for cylindrical spreading loss, so that the amplitude will remain comparable at increasing range.

The curved lines marked A1–A5 correspond to the bottom reflected energy which together with the deep refracted waves (D) converges and is re-focused in high intensity zones that is observed close to the surface in Fig. 8. A convergence-zone range of approximately 35 km causes the high intensity zones to appear at regular spatial intervals along the D-arrival at approximately 35, 70, and 105 km.

After about 20 km the deep refracted and bottom reflected waves overtake the surface channel arrival (B). The second reflected bottom reflection (A2) then start to appear, before it also overtakes the surface channel arrival just after 40 km. As can be seen from the steep change in arrival time for the bottom reflected arrivals their travel time is very sensitive to range.

Traces of slightly deeper sound channel arrivals can be seen as straight lines (e.g., C) arriving prior to the main surface channel arrival (B). The deeper channels can be seen in Fig. 8 as the deeper, partially overlapping, surface channels, where the main surface channel arrival (B) is limited to ca. 100 m depth, and deeper waves turn at approximately 220 m. The deeper sound channels have longer paths, but travel at greater speed.

In order to distinguish the deep refracted waves (D) with the bottom reflected waves (A) an additional simulation was performed using Case a with an ocean half-space. In this

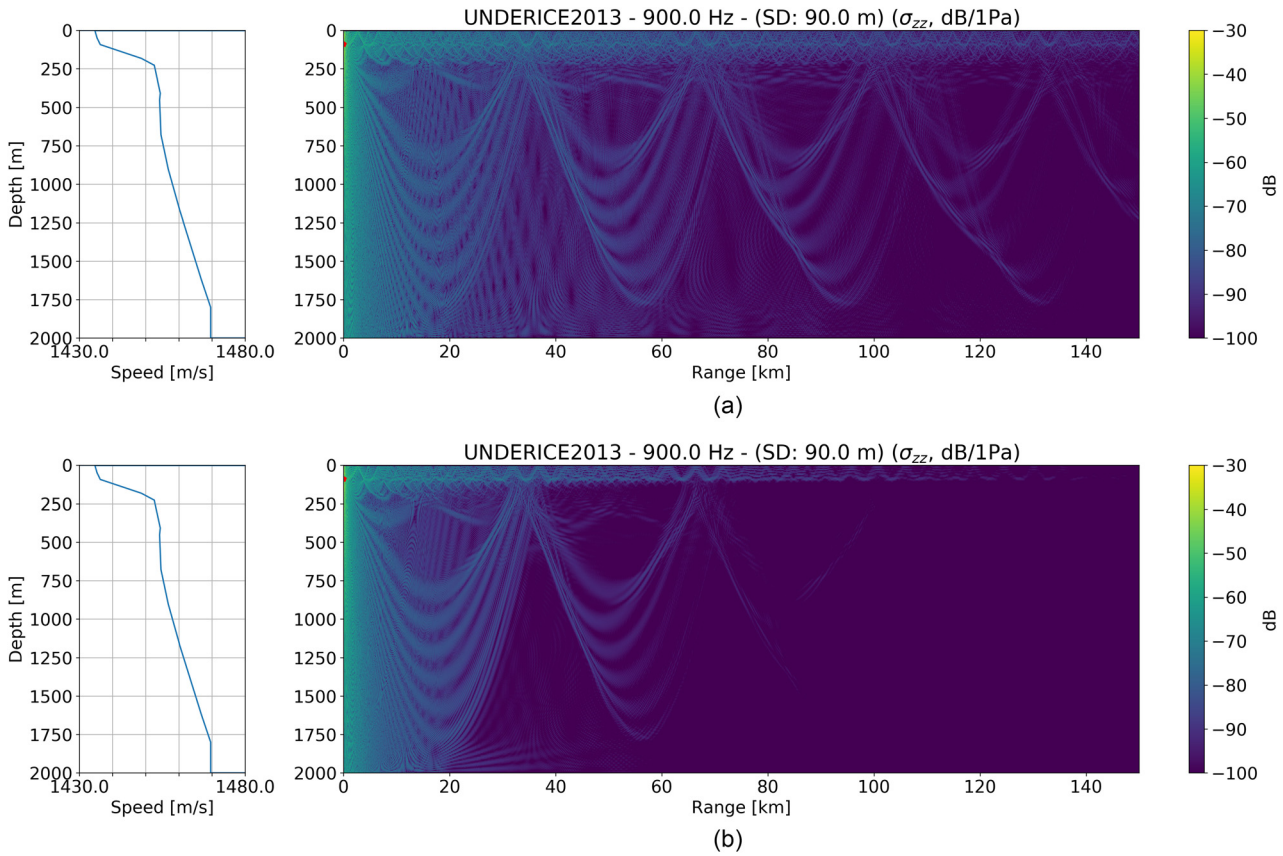

FIG. 8. (Color online) General propagation pattern: Transmission loss at 900 Hz for a source located at 90 m depth, calculated using OASES for the sound speed profile shown in Fig. 3 with a 2 m thick ice layer. The top panel shows TL for smooth ice, while the lower panel shows the result for sea-ice with 0.6 m RMS roughness and 19.1 m correlation length. A flat, reflecting sea-floor is used in the model.

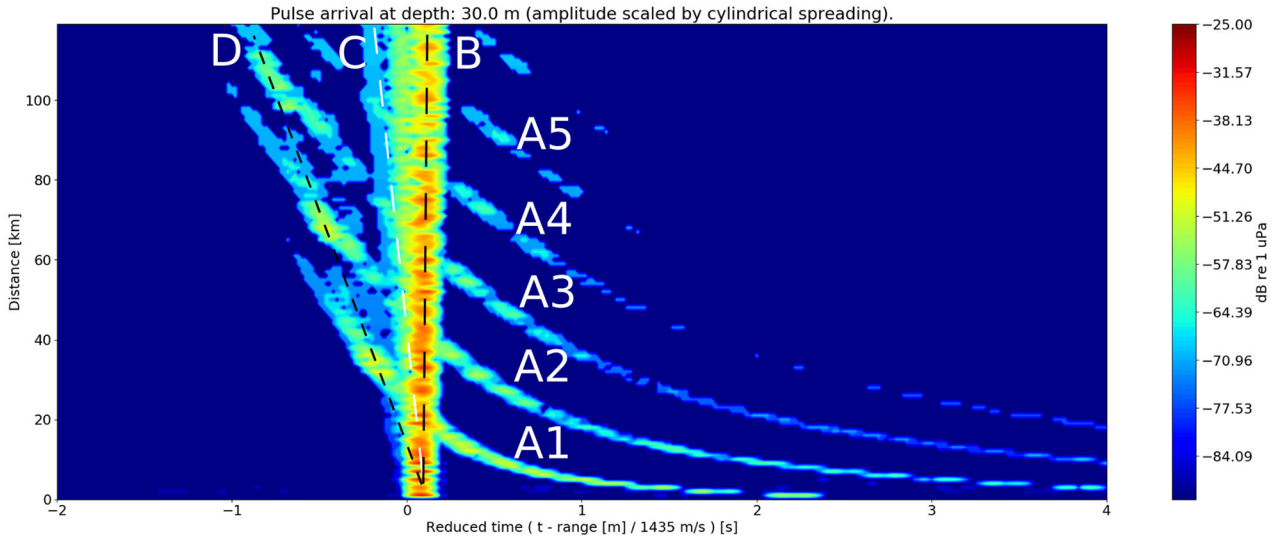

FIG. 9. (Color online) Matched filter output for the modeled signal for no ice (Case a), shown as a function of reduced time and range. The pulse is propagated from a source at 90 m depth to a receiver at 30 m depth for increasing range (r). Each pulse is time-shifted forward (leftward) with the travel-time at its range for the direct path in the surface channel: $\tau = t - r/c_0$, where $c_0 = 1435$ m/s is the lowest sound speed in the surface channel. The pulses are stacked vertically with the pulse received at 0 km at the bottom and the pulse received at 120 km at the top. The amplitude of each pulse is scaled with $\sqrt{r}$ to compensate for cylindrical spreading loss, so that the amplitude will remain comparable at increasing range.

case, the refracted waves arrived approximately at the same time as the bottom reflected waves at ranges near 35 km.

Figure 10 shows a similar plot for Case b (2 m smooth ice), Case c (0.2 m RMS, 2 m ice), and Case d (0.6 m RMS, 2 m ice).

Adding a 2 m smooth ice layer (Case b) to the model causes several weak arrivals slightly faster than the surface channel arrival to emerge. However, the effect of a change from a surface with no ice (Case a) to one with ice (Case b), is not dramatic. Transmission loss in the Arctic is sometimes assumed to be caused by a thicker ice layer. However, Fig. 5 show that increasing the thickness of the ice layer will have little effect on the reflection coefficient for incidence angles above 75°. The correlation between thicker ice and older (MY-ice), which has had more time to undergo deformation, and therefore likely is rougher could therefore indirectly account for the weakened signal.

The middle panel shows the pulse propagation for 0.2 m RMS (Case c) rough ice, at this point some weakening of the surface channel arrival becomes apparent at increased range compared to smooth ice. Some of the bottom reflections also become weakened. The surface channel arrival contains much energy and while it is weakened more than deep refracted (D) and bottom reflected waves it still appears strong in this plot. The bottom reflection and deep refracted waves that have not interacted with the sea-ice (no multiple reflections) remain almost intact (some loss can be attributed to loss of constructive interference from other paths).

As the roughness is increased to 0.6 m RMS in the lowermost panel it becomes more apparent that the bottom reflected and deep refracted waves that interact with the ice are almost lost, while the surface duct arrival is significantly weakened. The faster arrivals arising from waves traveling in the deeper surface channels (e.g., $D = 220$ m) disappear or are weakened as the roughness is increased.

Increasing roughness causes all waves that interact with the sea-ice to be weakened as they are scattered off the rough sea-ice, while those that do not interact remain almost intact. Some waves disappear before the surface channel arrival, even though they interact less with the sea-ice per range, because they contain less energy.

V. ANALYSIS OF RECEIVED SIGNAL STRUCTURE

In order to compare observations and signal, the received signals are time-shifted and stacked so that the signal structure can be studied, and they can be compared with the simulations. A representative mean signal is then extracted and compared with the simulations in Sec. VI.

In Fig. 11 the arrivals have been stacked such that the first arrival (bottom reflection, A1, or deep refraction, D) is aligned to $t = 0$ s. Arrival A1 was chosen as reference, as opposed to arrival B (surface channel arrival) in Figs. 9 and 10, because it is the most visible arrival throughout the data set. The arrivals were time-shifted by automatically matching the model output (of Case c) at the transmission distance with the received signal using the model synthetic signal as a matched filter template. This method generally performs better than attempts at manually identifying and picking the arrival, or simply using the maximum amplitude, which is sometimes the first and sometimes the second arrival.

The automatically time-shifted arrivals for hours 12–15 and 30–32 were then additionally manually adjusted. The manual adjustment was necessary because the same arrival is not always the strongest. However, by using the context of the previous and the following signal, and the smoothed and enhanced matched filter output, the correct reference arrival can be picked more easily. A more advanced selection algorithm might be used to select the correct arrival automatically, especially if absolute or relative travel times are available.

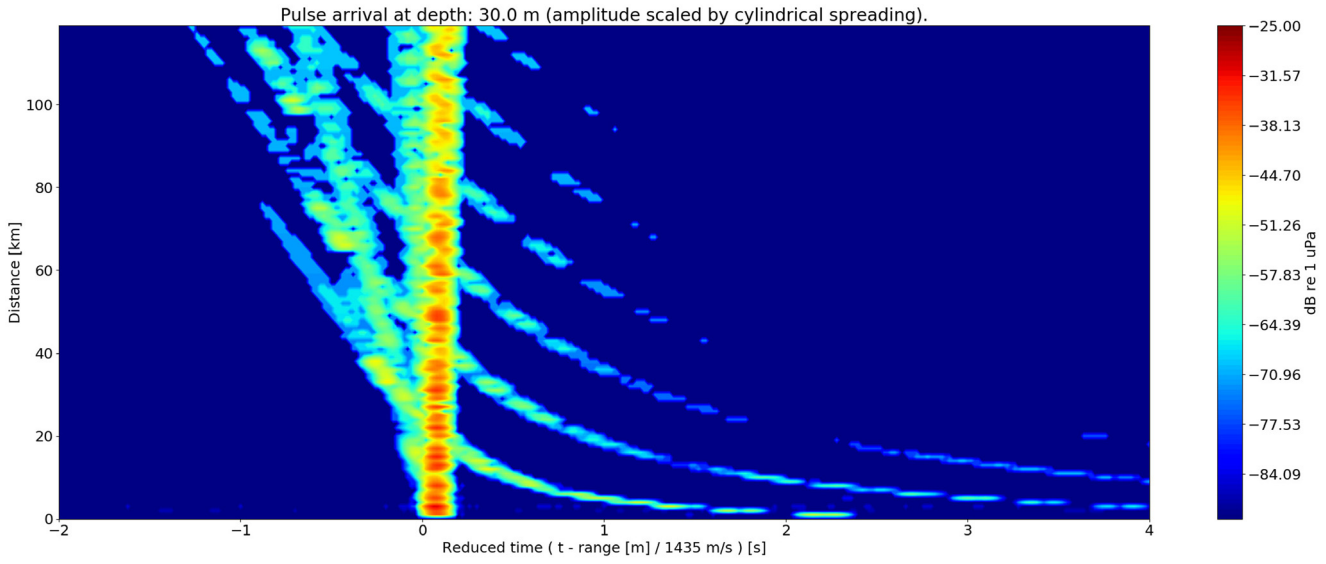

(a)

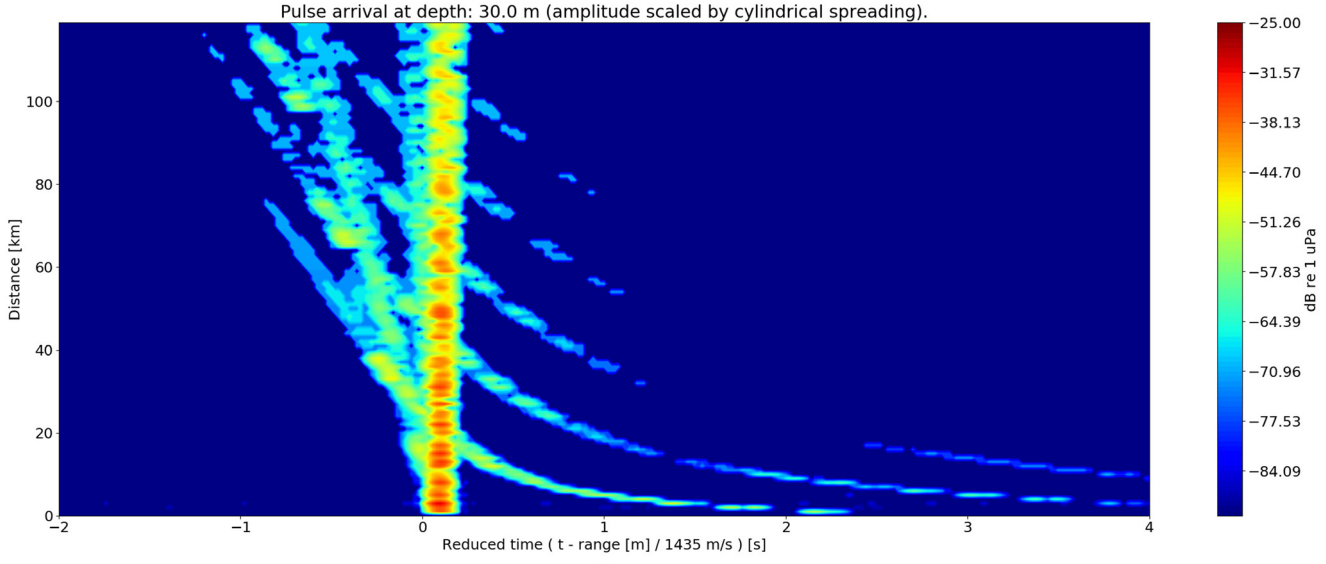

(b)

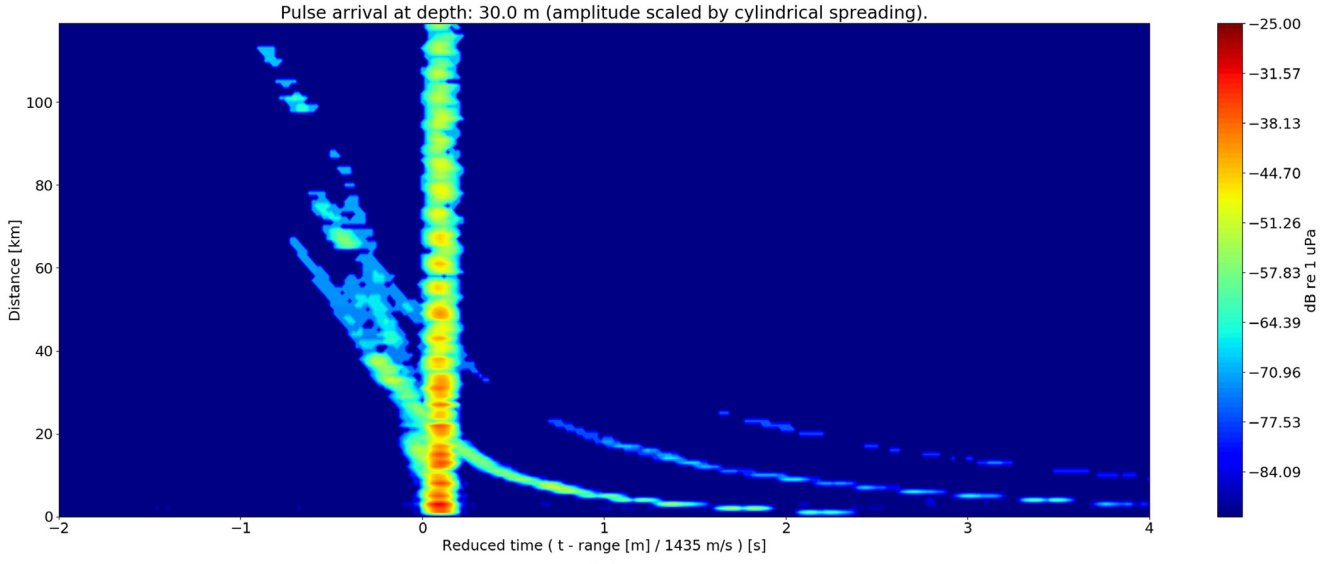

(c)

FIG. 10. (Color online) Equivalent plots to Fig. 9 for 2 m smooth ice (Case b), 2 m rough sea-ice (0.2 m RMS, Case c), and 2 m rough sea-ice (0.6 m RMS, Case d).

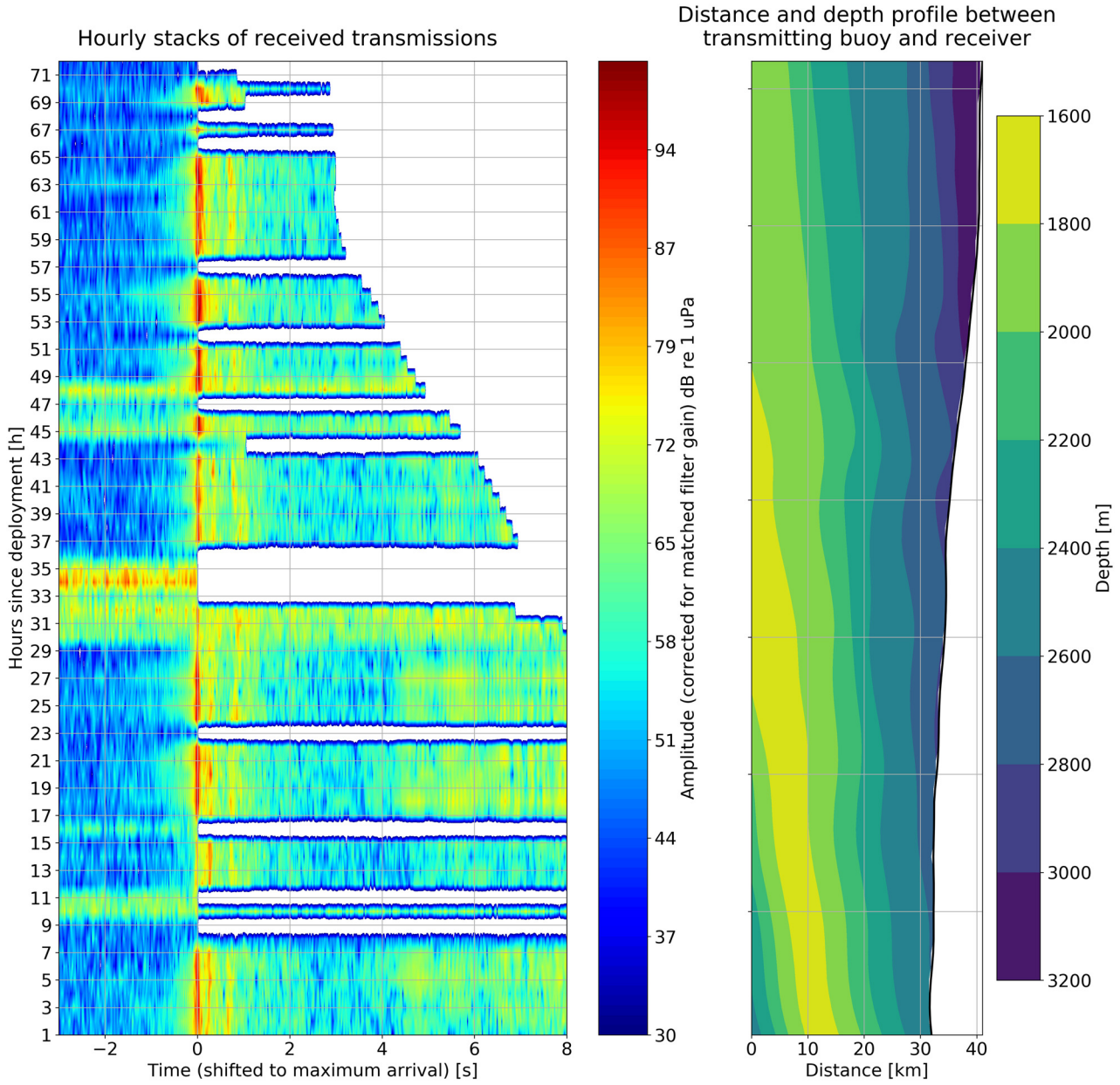

FIG. 11. (Color online) The received signals from Fig. 2 have been correlated with the synthetic signal (synthetics calculated at 1 km intervals). The maximum correlation is used as a reference to time-shift the received signal in order to get a better alignment than simply using the maximum amplitude. Hours 12–15 and 30–32 were manually adjusted in addition to this, since the first arrival in these cases were so weak that the maximum correlation occurred at the second arrival, and not the first as it does for the rest of the transmissions.

In Fig. 11, it can be seen that the bottom reflected arrivals A1 and A2 are visible throughout the experiment, while the surface channel arrival is less persistent. For hours 12–15 the surface channel arrival (B) is stronger than A1, otherwise A1 is the most stable arrival. The deep refracted arrival (D) is difficult to identify.

The surface channel arrival remains visible for the first 25 h, though some instability is apparent at hours 18 to 22. After the 25 h mark it is weakened, and only visible in a few of the segments before it disappears entirely at a distance of 39 km. The change in surface channel arrival stability and strength occurs as the network drifts apart from 32 to 39 km. The waves trapped in the surface channel are significantly affected by the sea-ice since they are continuously being reflected off the underside of the ice. As the range is increased waves in the surface channel undergo additional scattering and the arrival is weakened. The disappearance of the surface channel arrival could also be partly attributed to oceanographic variability, or the buoys drifting into different oceanographic conditions. Additional observations would be required to more precisely separate the effects of the ocean and ice on the signal structure.

VI. COMPARISON OF OBSERVATIONS WITH SIMULATIONS

In order to find a representative signal that could be compared with the synthetic signal, $N = 15$ transmissions between 32.0 ± 1.0 km (hours 1 to 19, with faulty transmissions omitted) were collected and time shifted in the same

way as in Fig. 11. Under the assumption that the signal structure does not change much within this range interval, the mean was calculated across the amplitudes of the transmissions. If the signal structure does not vary greatly, the coherent structure should be enhanced by calculating the mean. The mean was then used as a representative signal which could be qualitatively compared to the synthetic signal.

Model simulations for Case b, c, and d (Table III) are shown in Fig. 12 together with the mean of the signals calculated across the amplitudes of the 15 transmissions. The synthetic traces have been synchronized to the surface duct arrival (B) of the signals by using reduced time as in Figs. 9 and 10. The amplitude of arrival B in model Case b has been scaled to match the mean amplitude (75.6 dB re 1 μPa) of the corresponding arrival in the data. The result from the other model cases have been scaled by the same factor as Case b so that they can be compared with each other. Case a is not included as phase changes from the different model (without a sea-ice layer) could cause a different interference pattern and make it unsuitable for direct comparison with the sea-ice cases.

During this experiment, the sea-ice in the relevant area consisted of small (20–100 m) floes and it is unlikely that the floes are coupled well enough for waves to propagate coherently any longer than individual ice floes. Beam displacement is therefore not a likely effect in the measured signal. Beam displacement is accounted for in the OASES model, but due to the near total reflection, very little energy enters the sea-ice.

In Fig. 12, the deep refracted waves (D) become easier to discern compared to each single observation in Fig. 11. The bottom reflection (A1) and refracted arrival (D) arrive with approximately 0.1 s difference in the observations, while A1 and B (surface channel arrival) arrive with approximately 0.25 s separation. The delay between A1 and B matches quite well between observations and model, but the delay between A1 and D is too small compared to the observations. The second bottom arrival (A2) arrives too early in the model, possibly because of the simplified bathymetry in the model. The somewhat arbitrarily chosen seafloor parameters, and the fact that the obliquely sloping seafloor is assumed to be flat in OASES, increases uncertainty about the relative amplitude between A1 and B in the modeled signals. Arrival D is not directly affected by the seafloor.

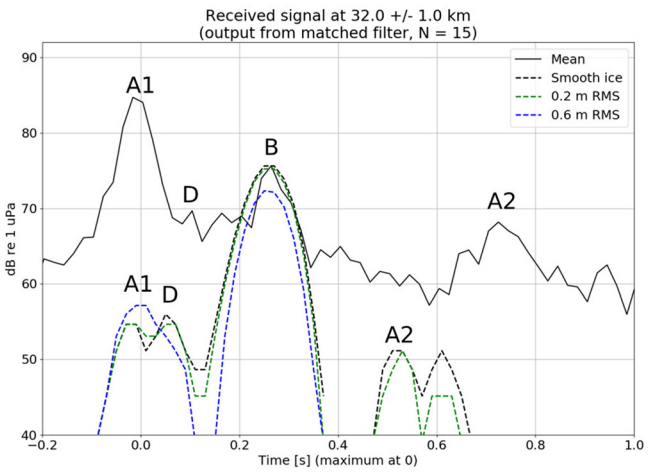

FIG. 12. (Color online) Mean of 15 time-synchronized received signals at distance 32.0 ± 1.0 km (as shown stacked in Fig. 11). The dashed lines show the synthetic signals computed by OASES at a range of 32 km for different cases. Labels A1, D, B, and A2 show the identified arrivals; first bottom reflection, refracted, surface duct arrival, and second bottom reflection for the measured data (top) and model (bottom) respectively. Data gaps (e.g., hours 8–11) are not included in the mean.

Figure 12 shows that A1 has greater relative amplitude than B for the observed signals, while all model cases show a weaker A1 than B arrival. However, increasing the roughness in the model causes A1 to gain amplitude relative to the surface duct arrival. This indicates both that increased roughness weakens the surface duct arrival more than the bottom reflected and deep refracted arrival, and that the roughness is greater in reality than the 0.6 m RMS. The weakened surface duct arrival in the model must therefore be caused by increased scattering from the sea-ice, and should be further weakened by greater and more realistic roughness than 0.6 m RMS.

Note that the model signals are scaled with the amplitude of the B arrival in Case b, so that if Case d was scaled in the same way; its B arrival would be matched with the signal B arrival, and the A1 arrival would be about 3 dB higher as well. This would further reduce the discrepancy in relative amplitude strength between A1 and B in observations and model.

For smooth sea-ice, the best propagation conditions can be found in the surface channel, but both model and data suggest that it is rapidly scattered when the sea-ice gets rougher. This may make interpretation of signals easier as there will be fewer multi-paths, but eventually the propagation pattern in the upper few 100 m will be characterized by shadow zones and high intensity zones (visible at, e.g., 35 km in Fig. 8). As the sea-ice gets rougher, the surface channel does not offer greater reception than the rest of the water column. Ignoring the roughness when modeling a setup either for communication or navigation will therefore overestimate the relative strength of the surface channel arrival when it may be weaker or not present at all.

VII. CONCLUSION

Observations of long-range acoustic signals in the Fram Strait Marginal Ice Zone in September 2013 are compared with simulations. The observations were made for ranges 32 to 41 km, while the simulations made using the OASES package covered ranges from 0 to 120 km. Previous measurements of acoustic and elastic properties of sea-ice were used to establish a realistic description of the sea-ice layer. A sound speed profile was derived from XCTD measurements, while the elastic parameters of the flat seafloor are based on seismic observations from the Fram Strait. These environmental parameters were used as input to the acoustic model. Simulations of reflection coefficients (1–1500 Hz) and pulse propagation (870–930 Hz) were made without ice, smooth ice, and increasingly rough sea-ice. Transmission loss (900 Hz) was calculated for smooth ice and rough sea-ice.

Observations and simulations show a clear weakening of the waves that are trapped in the surface channel with increasing range. The deeper refracted and reflected waves which interact less with the sea-ice are relatively less weakened than the surface trapped acoustic waves. The observed weakening of the waves trapped in the surface duct is attributed to the roughness of the sea-ice rather than other sea-ice characteristics. This is because the waves trapped in the surface channel have incidence angles above 75° and therefore experience close to total reflection at a smooth sea-ice interface. Introducing a rough interface increases the scattering loss for all incidence angles and can explain the observed loss (Fig. 5). Consequently, for ranges above approximately 30 km, and for 900 Hz signals, the roughness is the most significant characteristic of the sea-ice for acoustic propagation. Waves with lower frequency or lower incidence angles can be more greatly affected by the elastic parameters of the sea-ice. Lower incidence angles occur for short ranges, or for a deeper surface duct.

The method of small perturbations used to model roughness in OASES have been shown to work well for long wavelengths compared to the scale of the roughness.[30] For sea-ice parameters used in this work the method is found to be limited to a roughness less than approximately 0.6 m RMS for 900 Hz. However, this is less than the estimated roughness from ice draft measurements and the corresponding simulations underestimate the dampening of the waves trapped in the surface duct in comparison with the observations.

Lack of high resolution sea-ice thickness measurements and observations of elastic properties limits comparison with acoustic experiments and the understanding of long-range under-ice acoustic propagation. Further progress can be made by improving theory and numerical solutions to handle scattering from rougher sea-ice in long-range problems.

ACKNOWLEDGMENTS

We thank the Norwegian Coast Guard for allocating ship time on the icebreaker K.V. Svalbard to the UNDER-ICE project. Captain Roar Lund and the ship's crew provided excellent and enthusiastic support during the field operations. We thank Peter Worcester and his acoustic group at the Scripps Institution of Oceanography for assistance with the acoustic instrumentation, and Peter Koski of Woods Hole Oceanographic Institution for deployment and recovery of the acoustic buoys. G.H. would like to express his appreciation for the invitation to stay at WHOI and the fruitful discussions that this enabled with the acoustic engineering group and the modeling group there. We acknowledge M. Babiker (NERSC) (Ref. 23) as author of the satellite imagery figure (in Fig. 1). We thank H. Schmidt for taking the time to discuss and answer questions concerning the OASES model. The fieldwork was performed under funding from the Research Council of Norway through the UNDER-ICE (Grant No. 226373) project and ENGIE E&P Norway providing additional support. The data analysis, modeling and preparation of the publication has been carried out under funding from the Office of Naval Research (Global) (Grant No. N62909-14-1-NO33) and UNDER ICE (Grant No. 226373) projects. The U.S. Office of Naval Research provided partial support for this work under Grant No. N000141210176 to the Woods Hole Oceanographic Institution. Any opinions, findings, and conclusions or recommendations expressed in this publication are those of the authors and do not necessarily reflect the views of the Office of Naval Research.

[1]O. M. Johannessen, H. Sagen, S. Sandven, and K. V. Stark, "Hotspots in ambient noise caused by ice-edge eddies in the Greenland and Barents seas," IEEE J. Ocean. Eng. **28**, 212–228 (2003).
[2]C. Strong and I. G. Rigor, "Arctic marginal ice zone trending wider in summer and narrower in winter," Geophys. Res. Lett. **40**, 4864–4868, doi:10.1002/grl.50928 (2013).
[3]J. A. Johannessen, O. M. Johannessen, E. Svendsen, R. Shuchman, T. Manley, W. J. Campbell, E. G. Josberger, S. Sandven, J. C. Gascard, T. Olaussen, K. Davidson, and J. Van Leer, "Mesoscale Eddies in the Fram Strait marginal ice zone during the 1983 and 1984 marginal ice zone experiments," J. Geophys. Res. Ocean. **92**, 6754–6772, doi:10.1029/JC092iC07p06754 (1987).
[4]S. G. Gallaher, T. P. Stanton, W. J. Shaw, S. T. Cole, J. M. Toole, J. P. Wilkinson, T. Maksym, and B. Hwang, "Evolution of a Canada Basin ice-ocean boundary layer and mixed layer across a developing thermodynamically forced marginal ice zone," J. Geophys. Res. Ocean. **121**, 6223–6250, doi:10.1002/2016JC011778 (2016).
[5]F. B. Jensen, W. A. Kuperman, M. B. Porter, H. Schmidt, and J. F. Bartram, *Computational Ocean Acoustics*, 2nd ed. (Springer, New York, 2011), 794 pp.
[6]I. Dyer, P. H. Dahl, A. B. Baggeroer, and P. N. Mikhalevsky, "Ocean dynamics and acoustic fluctuations in the Fram Strait marginal ice zone," Science **236**, 435–436 (1987).
[7]P. H. Dahl, A. B. Baggeroer, P. N. Mikhalevsky, and I. Dyer, "Measurement of the temporal fluctuations of cw tones propagated in the marginal ice zone," J. Acoust. Soc. Am. **83**, 2175–2179 (1988).
[8]P. F. Worcester, J. F. Lynch, W. M. L. Morawitz, R. Pawlowicz, P. J. Sutton, B. D. Cornuelle, O. M. Johannessen, W. H. Munk, W. B. Owens, R. Shuchman, and R. C. Spindel, "Evolution of the large-scale temperature field in the Greenland Sea during 1988-89 from tomographic measurements," Geophys. Res. Lett. **20**, 2211–2214, doi:10.1029/93GL02373 (1993).
[9]G. Jin, J. F. Lynch, R. Pawlowicz, and P. Worcester, "Acoustic scattering losses in the Greenland Sea marginal ice zone during the 1988-89 tomography experiment," J. Acoust. Soc. Am. **96**, 3045–3053 (1994).
[10]L. E. Mellberg, O. M. Johannesen, D. N. Connors, G. Botseas, and D. G. Browning, "Acoustic propagation in the western Greenland Sea frontal zone," J. Acoust. Soc. Am. **89**, 2144–2156 (1991).
[11]H. Sagen, P. F. Worcester, M. A. Dzieciuch, F. Geyer, S. Sandven, M. Babiker, A. Beszczynska-Möller, B. D. Dushaw, and B. D. Cornuelle, "Resolution, identification, and stability of broadband acoustic arrivals in Fram Strait," J. Acoust. Soc. Am. **141**, 2055–2068 (2017).
[12]P. H. Dahl, "Acoustic diffraction from a semi-infinite elastic plate under arbitrary fluid loading with application to scattering from Arctic ice leads," Ph.D. thesis, Woods Hole Oceanographic Institution and Massachusetts Institute of Technology, Cambridge, MA (1989).
[13]J. R. Fricke, "Acoustic scattering from elastic ice: A finite difference solution," Ph.D. thesis, Woods Hole Oceanographic Institution and Massachusetts Institute of Technology, Cambridge, MA (1991).
[14]P. N. Mikhalevsky, H. Sagen, P. F. Worcester, A. B. Baggeroer, J. Orcutt, S. E. Moore, C. M. Lee, K. J. Vigness-Raposa, L. Freitag, M. Arrott, K. Atakan, A. Beszczynska-Möller, T. F. Duda, B. D. Dushaw, J. C. Gascard, A. N. Gavrilov, H. Keers, A. K. Morozov, W. H. Munk, M. Rixen, S. Sandven, E. Skarsoulis, K. M. Stafford, F. Vernon, and M. Y. Yuen, "Multipurpose acoustic networks in the integrated arctic ocean observing system," Arctic **68**, 1–17 (2015).
[15]O. I. Diachok, "Effects of sea-ice ridges on sound propagation in the Arctic Ocean," J. Acoust. Soc. Am. **59**, 1110–1120 (1976).
[16]P. Mikhalevsky, "Acoustics, Arctic," in *Encyclopedia of Ocean Sciences*, 2nd ed., edited by J. H. Steele, K. K. Turekian, and S. A. Thorpe (Academic Press, London, 2001), pp. 53–61.

[17]B. E. Miller and H. Schmidt, "Observation and inversion of seismo-acoustic waves in a complex arctic ice environment," J. Acoust. Soc. Am. **89**, 1668–1685 (1991).
[18]D. F. McCammon and S. T. McDaniel, "The influence of the physical properties of ice on reflectivity," J. Acoust. Soc. Am. **77**, 499–507 (1985).
[19]K. D. LePage and H. Schmidt, "Modeling of low-frequency transmission loss in the central Arctic," J. Acoust. Soc. Am. **96**, 1783–1795 (1994).
[20]W. A. Kuperman and H. Schmidt, "Self consistent perturbation approach to rough surface scattering in stratified elastic media," J. Acoust. Soc. Am. **86**, 1511–1522 (1989).
[21]H. Schmidt and F. B. Jensen, "A full wave solution for propagation in multilayered viscoelastic media with application to Gaussian beam reflection at fluid solid interfaces," J. Acoust. Soc. Am. **77**, 813–825 (1985).
[22]L. Freitag, P. Koski, A. Morozov, S. Singh, and J. Partan, "Acoustic communications and navigation under Arctic ice," in *2012 OCEANS*, Hampton Roads, VA (IEEE, 2012), pp. 1–8.
[23]F. Geyer, H. Sagen, G. Hope, M. Babiker, and P. F. Worcester, "Identification and quantification of soundscape components in the marginal ice zone," J. Acoust. Soc. Am. **139**, 1873–1885 (2016).
[24]J. R. Klauder, A. C. Price, S. Darlington, and W. J. Albersheim, "The theory and design of chirp radar," Bell Syst. Tech. J. **39**, 745–808 (1960).
[25]M. Jakobsson, L. Mayer, B. Coakley, J. A. Dowdeswell, S. Forbes, B. Fridman, H. Hodnesdal, R. Noormets, R. Pedersen, M. Rebesco, H. W. Schenke, Y. Zarayskaya, D. Accettella, A. Armstrong, R. M. Anderson, P. Bienhoff, A. Camerlenghi, I. Church, M. Edwards, J. V. Gardner, J. K. Hall, B. Hell, O. Hestvik, Y. Kristoffersen, C. Marcussen, R. Mohammad, D. Mosher, S. V. Nghiem, M. T. Pedrosa, P. G. Travaglini, and P. Weatherall, "The International Bathymetric Chart of the Arctic Ocean (IBCAO) Version 3.0," Geophys. Res. Lett. **39**, L12609, doi:10.1029/2012GL052219 (2012).
[26]W. Jokat, E. Weigelt, Y. Kristoffersen, T. Rasmussen, and T. Schöne, "New geophysical results from the south-western Eurasian Basin (Morris Jesup Rise, Gakkel Ridge, Yermak Plateau) and the Fram Strait," Geophys. J. Int. **123**, 601–610 (1995).
[27]T. Lavergne, S. Eastwood, Z. Teffah, H. Schyberg, and L. A. Breivik, "Sea ice motion from low-resolution satellite sensors: An alternative method and its validation in the Arctic," J. Geophys. Res. Ocean. **115**, C10032, doi:10.1029/2009JC005958 (2010).
[28]H. Schmidt, "SAFARI: Seismo-Acoustic Fast Field Algorithm for Range-Independent Environments. User's Guide," Tech. Rep. (SACLANT Undersea Research Centre, San Bartolomeo, Italy, 1988).
[29]F. R. DiNapoli and R. H. Mellen, "Low frequency attenuation in the Arctic Ocean," in *Ocean Seismo-acoustics: Low-Frequency Underwater Acoustics*, edited by T. Akal and J. M. Berkson (Plenum Press, New York, 1986), pp. 387–395.
[30]W. A. Kuperman and H. Schmidt, "Rough surface elastic wave scattering in a horizontally stratified ocean," J. Acoust. Soc. Am. **79**, 1767–1777 (1986).
[31]National Snow and Ice Data Center, "Submarine upward looking sonar ice draft profile data and statistics, version 1" (National Snow and Ice Data Center, Boulder, CO, 1998), available at 10.7265/N54Q7RWK (Last viewed May 1, 2017).
[32]D. K. Dacol and D. H. Berman, "Sound scattering from a randomly rough fluid-solid interface," J. Acoust. Soc. Am. **84**, 292–302 (1988).
[33]E. Hansen, S. Gerland, M. A. Granskog, O. Pavlova, A. H. H. Renner, J. Haapala, T. B. Løyning, and M. Tschudi, "Thinning of Arctic sea ice observed in Fram Strait: 1990-2011," J. Geophys. Res. Oceans **118**, 5202–5221, doi:10.1002/jgrc.20393 (2013).
[34]H. Laible and S. D. Rajan, "Temporal evolution of under ice reflectivity," J. Acoust. Soc. Am. **99**, 851–865 (1996).
[35]D. Rajan, G. V. Frisk, J. A. Doutt, and J. Sellers, "Determination of compressional wave and shear wave speed profiles in sea ice by crosshole tomography - Theory and experiment," J. Acoust. Soc. Am. **93**, 721–738 (1993).
[36]T. E. Clee, J. C. Savage, and K. G. Neave, "Internal friction in ice near its melting point," J. Geophys. Res. **74**, 973–980, doi:10.1029/JB074i004p00973 (1969).
[37]H. Hobæk and H. Sagen, "On underwater sound reflection from layered ice sheets," in *Proceedings of the 39th Scandinavian Symposium on Physical Acoustics*, Geilo, Norway, arXiv:1604.02247 (2016).
[38]M. Kimura and T. Tsurumi, "Characteristics of acoustic wave reflection from the transition layer of surficial marine sediment," Proc. 2002 Int. Symp. Underwater Technology **2002**, 225–230.
[39]M. A. Biot, "Theory of propagation of elastic waves in a fluid-saturated porous solid. II. Higher frequency range," J. Acoust. Soc. Am. **28**, 168–178 (1956).
[40]M. A. Biot, "Theory of propagation of elastic waves in a fluid-saturated porous solid. I. Low-frequency range," J. Acoust. Soc. Am. **28**, 179–191 (1956).
[41]M. B. Porter, "The BELLHOP Manual and User's Guide (Preliminary Draft)," Tech. Rep. (Heat, Light, and Sound Research, Inc., La Jolla, CA, 2011).